Accepted Manuscript

Hydrogen induced structure and property changes in Eu_3Si_4

Gustav Ek, Reji Nedumkandathil, Robert Johansson, Jorge Montero, Claudia Zlotea, Mikael S. Andersson, Per Nordblad, Chiu Tang, Martin Sahlberg, Ulrich Häussermann

PII: S0022-4596(19)30262-2

DOI: https://doi.org/10.1016/j.jssc.2019.05.033

Reference: YJSSC 20776

To appear in: *Journal of Solid State Chemistry*

Received Date: 20 March 2019

Revised Date: 19 May 2019

Accepted Date: 19 May 2019

Please cite this article as: G. Ek, R. Nedumkandathil, R. Johansson, J. Montero, C. Zlotea, M.S. Andersson, P. Nordblad, C. Tang, M. Sahlberg, U. Häussermann, Hydrogen induced structure and property changes in Eu_3Si_4, *Journal of Solid State Chemistry* (2019), doi: https://doi.org/10.1016/j.jssc.2019.05.033.

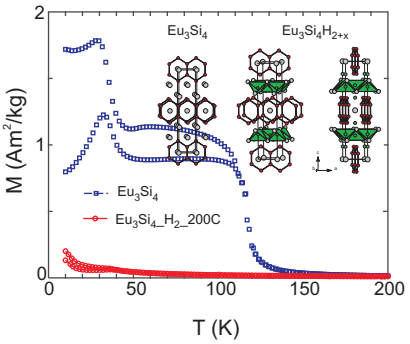

Hydrogen Induced Structure and Property Changes in Eu_3Si_4

Gustav Ek[a], Reji Nedumkandathil[b], Robert Johansson[c], Jorge Montero[d], Claudia Zlotea[d], Mikael S. Andersson[e,**], Per Nordblad[e], Chiu Tang[f], Martin Sahlberg[a], Ulrich Häussermann[b,*]

[a]*Department of Chemistry - Ångström laboratory, Uppsala University, Sweden*

[b]*Department of Materials and Environmental Chemistry, Stockholm University, Sweden*

[c]*Department of Physics and Astronomy, Uppsala University, Sweden*

[d]*Université Paris Est, Institut de Chimie et des Matériaux Paris-Est, CNRS, France*

[e]*Department of Engineering Sciences, Uppsala University, Sweden*

[f]*Diamond Light Source, Harwell Science and Innovation Campus, UK*

[*]Ulrich.Haussermann@mmk.su.se

[**]Present address: Department of Chemistry and Chemical Engineering, Chalmers University of Technology, Sweden

Abstract

Hydrides $Eu_3Si_4H_{2+x}$ were obtained by exposing the Zintl phase Eu_3Si_4 to a hydrogen atmosphere at a pressure of 30 bar and temperatures from 25 to 300 °C. Structural analysis using powder X-ray diffraction (PXRD) data suggested that hydrogenations in a temperature range 25 – 200 ºC afford a uniform hydride phase with an orthorhombic structure (*Immm*, $a \approx$ 4.40 Å, $b \approx$ 3.97 Å, $c \approx$ 19.8 Å), whereas at 300 ºC mixtures of two orthorhombic phases with $c \approx$ 19.86 and ≈19.58 Å were obtained. The assignment of a composition $Eu_3Si_4H_{2+x}$ is based on first principles DFT calculations, which indicated a distinct crystallographic site for H in the Eu_3Si_4 structure. In this position, H atoms are coordinated in a tetrahedral fashion by Eu atoms. The resulting hydride $Eu_3Si_4H_2$ is stable by -0.46 eV/H atom with respect to Eu_3Si_4 and gaseous H_2. Deviations between the lattice parameters of the DFT optimized $Eu_3Si_4H_2$ structure and the ones extracted from PXRD patterns pointed to the presence of additional H in interstitials also involving Si atoms. Subsequent DFT modeling of compositions $Eu_3Si_4H_3$ and $Eu_3Si_4H_4$ showed considerably better agreement to the experimental unit cell volumes. It was then concluded that the hydrides of Eu_3Si_4 have a composition $Eu_3Si_4H_{2+x}$ ($x < 2$) and are disordered with respect to H in Si_2Eu_3 interstitials. Eu_3Si_4 is a ferromagnet with a T_C at about 120 K. Ferromagnetism is effectively quenched in $Eu_3Si_4H_{2+x}$. The effective magnetic moment for both materials is 7.5 μ_B which is typical for compounds containing Eu^{2+} $4f^7$ ions.

Keywords: Zintl phases, Zintl phase hydrides, rare earth metal silicides, magnetic properties

1. Introduction

Zintl phases, which are composed of an active metal (i.e. alkali, alkaline earth, or rare earth) and a more electronegative p-block metal or semimetal, represent a large family of inorganic compounds [1-3]. As their characteristic feature, atoms of the electronegative component appear reduced and may form polyanionic structures to achieve an octet. Like many intermetallic compounds Zintl phases can react with hydrogen to form hydrides. However, the rather high ionicity of Zintl phases makes such hydrides peculiar. Hydrogen takes an ambivalent role and can be incorporated in two principal ways: either hydridic, where H is exclusively coordinated by active metals (interstitial hydrides), or as part of the polyanion where it acts as a covalently bonded ligand (polyanionic hydrides) [4,5]. Chemical structures and physical properties of Zintl phases can change profoundly upon H incorporation. This provides interesting prospects for fundamental inorganic chemistry and materials science.

Well investigated are the hydrogenation induced metal–semiconductor transitions for the systems MTrTt – MTrTtH (M = alkaline earth; Tr = Al, Ga, In; Tt = Si, Ge, Sn). Here charge imbalanced AlB_2-type related Zintl phases form charge balanced semiconductor hydrides in which H is bonded to Tr and thus part of the polyanion [6,7]. Further, it has been shown that CrB-type related Zintl phases MTt can be hydrogenated to yield hydrides $MTtH_{1+x}$ with x ~0.33, ~0.67, and ~0.87 featuring novel ribbon- and chain-like polyanions $[Tt_3H]^{3-}$, $[Tt_2H]^{2-}$, and $[TtH]^{-}$ in which H is covalently bonded to a Tt element [8,9]. The discovery of polyanions with Tt–H bonds represented an important extension of Zintl phase hydrides. Another peculiar feature of $MTtH_{1+x}$ is the simultaneous presence of interstitial H which is exclusively coordinated by M and not bonded to Tt. The CrB structure type is also adopted for most rare earth (RE) monogallides, REGa, which – considering RE as trivalent – are isoelectronic to MTt. In contrast with MTt, the REGa compounds display cooperative magnetism. Recent studies on NdGa and GdGa showed that, similar to MTt, also REGa transform into hydrides $REGaH_{1+x}$ by incorporating H both interstitially (i.e. exclusively coordinated by RE atoms) and as part of a two-dimensional Ga-H polyanion. At the same time the magnetic interaction is changed from ferromagnetic to antiferromagnetic nature [10,11,12].

In this paper we report on the hydrogenation behavior of Eu_3Si_4. Eu_3Si_4 was first described in 2004 [13]. Its body centered orthorhombic crystal structure (space group *Immm*, #71) is depicted in Figure 1 [14]. Si atoms form hexagon rings, which in turn are condensed into one-dimensional ribbons that run in the *b* direction (Figure 1a). Following the Zintl concept, three-bonded (3b) Si atoms (henceforth termed Si1) carry a formal charge of -1, and two-bonded (2b) ones (henceforth termed Si2) carry a charge of -2. A polyanionic strand is composed of four Si atoms, 2 Si1 and 2 Si2 (there are two equivalent strands in the body centered unit cell). Thus, a strand $[Si1_2Si2_2]$ carries a formal charge of -6, which is balanced by Eu cations, provided they are in a +2 state. The divalent character of Eu was confirmed from magnetic measurements, which showed a magnetic moment in agreement with a $4f^7$ electron configuration when Eu_3Si_4 is in the paramagnetic state above 117 K [13]. Eu1 atoms are situated between Si hexagon rings. Eu2 atoms form arrays of edge condensed tetrahedra, which separate Si hexagon ribbons in the *c* direction. Both Eu atoms together provide a

trigonal prismatic coordination to Si atoms (Figure 1b). There is an apparent close relationship to the orthorhombic CrB structure (space group *Cmcm* #63), which is adopted by the REGa compounds (Figure 1b). Their structure is built from slabs of trigonal prims formed by the RE atoms, which host Ga atoms that are arranged as zigzag chains. The Eu_3Si_4 structure can be considered as built up from slabs of CrB structure (with a thickness *b*/2) with alternating [010] and [0-10] orientation. Condensing slabs at layers of common RE atoms will then connect zigzag chains into hexagon rings.

Eu_3Si_4 displays two magnetic transitions at 117 and 40 K [13]. The first one is attributed to a ferromagnetic ordering of the Eu2 atoms. This transition probably relates to the ferromagnetic transition in REGa compounds because RE atoms in REGa have the same structural arrangement as the Eu2 atoms in Eu_3Si_4. The Curie temperatures T_C of REGa are in a range 15 – 190 K [15,16,17]. The second transition in Eu_3Si_4 is caused by a ferromagnetic ordering of the Eu1 atoms, resulting in a net ferrimagnetic ground state. The ferromagnetic properties of Eu_3Si_4 must be a consequence of the coupling of magnetic moments arising from localized 4f electrons, which is mediated via conduction electrons. The validity of such a RKKY coupling mechanism, however, contradicts the description of Eu_3Si_4 as a charge balanced Zintl phase, because in this simple picture all valence electrons are localized as bonds and lone pairs within the Si polyanion, which would not leave any excess electrons for mediating ferromagnetic coupling. Again, this is similar to ferromagnetic REGa for which H incorporation triggers a transition from ferromagnetic to antiferrmomagnetic behavior [10,11]. In contrast with Eu_3Si_4, all RE atoms in REGa are crystallographically equivalent.

2. Methods

2.1. Synthesis

All steps of synthesis and sample preparation were carried out in an Ar-filled glove box. Eu (99.9%) and Si (99.999%) were purchased from ABCR. Eu_3Si_4 was prepared by arc-melting stoichiometric mixtures of Eu and Si. To ensure homogeneity, samples were re-melted five times and flipped between each melting. Slight changes in the stoichiometry or insufficient re-melting led to the presence of EuSi and $EuSi_2$ in the product. Most homogeneous samples Eu_3Si_4 were obtained when pre-reacting stoichiometric amounts of Eu and Si - enclosed in a Ta ampule - in an RF furnace for 2 h at about 1000 °C into a mixture of Eu_3Si_4, EuSi, and $EuSi_2$, and subsequently arc-melting this mixture. Buttons of Eu_3Si_4 from arc-melting were ground in an agate mortar and portions of 50–100 mg were pressed into pellets. The pellets were placed in an Al_2O_3 (corundum) crucible inside a custom-made stainless steel autoclave, which was subsequently pressurized to 30 bar with H_2 gas. The autoclave was then placed inside a tube furnace and hydrogenations performed at room temperature, 100, 200, and 300 °C for 24 h. The temperature inside the autoclave was monitored by a K-type thermocouple. Both Eu_3Si_4 and products obtained from its hydrogenation have a grey color and decompose when exposed to humid atmosphere. For purity check and phase analysis of samples, powder X-Ray diffraction (PXRD) was employed.

2.2. Pressure Composition Isotherm

Hydrogen absorption properties were measured by Pressure-Composition-Isotherm (PCI) curves with a commercial volumetric device (SETARAM PCT PRO) equipped with calibrated and thermalized volumes and pressure gauges at 25 °C. The sample holder corresponded to a stainless steel container closed with a metal seal and was inserted in a resistance furnace at 250 and 300 °C. High purity hydrogen (6N) was introduced step by step up to around 3 bar. Due to very slow kinetics, the time allowed for equilibrium was between 1500 and 2000 minutes per pressure point. It was compulsory to load the sample in an Ar-filled glove box in order to avoid air-exposure since surface oxidation resulted in a dramatic decrease of kinetics, with sometimes no absorption.

2.3. Structural Characterization of Eu_3Si_4 and hydrogenous Eu_3Si_4

PXRD patterns were collected on a Panalytical X'Pert PRO diffractometer operated with Cu either Cu $K\alpha_1$ (λ = 1.5406 Å) radiation in θ-2θ diffraction geometry. Powder samples were mounted on a Si wafer zero-background holder and sealed between kapton tape to ensure an oxygen/moisture free atmosphere during data collection. Data were measured in a 2θ range 10 – 90°. High-energy X-ray diffraction experiments were carried out for Eu_3Si_4 and products from hydrogenations at 200 and 300 ºC (Eu3Si4_H2_200C and Eu3Si4_H2_300C) at the beamline P02.1 at PETRAIII, DESY, which operates at a fixed energy of approximately 60 keV. The wavelength was determined to be 0.20727(6) Å by using a LaB_6 NIST standard. Powder samples were loaded in a glass capillary with 0.5 mm diameter. 2D diffraction images, each obtained through the accumulation of 20 frames with an exposure time of one second per frame, were collected with a Perkin Elmer amorphous silicon area detector

(XRD1621) placed at 329 mm from the sample. The 2D diffraction images were then integrated into a linear scattering signal with the software Fit2D and averaged [18]. The Rietveld method [19] as implemented in the FULLPROF program (v. 2.05, July 2011) [20] was used for structure and phase analysis. Structure refinements of synchrotron data were based on the established structure model for Eu_3Si_4. A six-coefficient polynomial refinement was used for the background. Lattice parameters were fitted with the value from structure model. The peak shape was modeled by Thompson-Cox-Hastings pseudo-Voigt axial divergence asymmetry. Fits could be considerably improved when applying a preferred orientation correction to the intensities parallel to (101).

2.4. In-situ diffraction

In-situ Synchrotron PXRD experiments were performed at the I11 beamline at the Diamond light source, UK using a wavelength of 0.49404 Å (as determined by a Si standard) and a wide-angle position sensitive detector based on Mythen-2 strip modules. The sample was loaded into a 0.7 mm quartz capillary that was mounted on a Norby type cell [21] and sealed using Epoxy. The cell was then mounted and leak checked with He gas before applying a pressure of 30 bar H_2. Data was collected at 20 s per scan during a heat-cool temperature program (RT – 400 °C – RT at 5 °C/min) using a hot-air blower. Consequently, the duration of the heating and cooling ramps were about 80 min. In between the ramps a short period of dwelling (5 min) was inserted. Data analysis was done by the Rietveld method implemented in the software TOPAS 6 academic [22] in sequential mode. Peak functions were described by the fundamental parameters approach and the background by a 6^{th} degree Chebychev polynomial. During sequential mode, unit cell parameters of three phases were refined (initial Eu_3Si_4, hydrogenous Eu_3Si_4, and the impurity phase $EuSi_2$) along with scale factors and background parameters. All other parameters were kept fixed.

2.5. Computations

DFT calculations were performed using the Vienna ab initio Simulation Package (VASP) [23,24] utilizing the projector augmented wave method (PAW) [25,26] to treat the interactions between the electrons and the nuclei. The generalized gradient approximation (GGA) in the parametrization of the Perdew-Burke-Ernzerhof (PBE) [27] approach was employed to approximate the exchange and correlation. The plane wave basis set was terminated at a kinetic energy cutoff of 400 eV. The conjugate gradient algorithm was used to relax the atomic nuclei positions to a local minimum in the total energy landscape until the global break condition of maximum 10^{-3} eV/Å of force between the atoms was reached. A 25×25×7 Monkhorst-Pack k-point mesh was used to sample the Brillouin zone[28] . Formation energies ΔE, referring to zero kelvin were calculated according to

$$\Delta E = (1/n)\,[E(Eu_3Si_4H_n) - E(Eu_3Si_4) - n/2\,E(H_2)]$$

where E denotes the total energy of the enclosed-in-parentheses system and n = 2,3,4. For the H_2 molecule, a box of $8\times8\times8 Å^3$ dimensions was used with Γ-point sampling of the Brillouin zone. Structure relaxations were carried out for the compositions $Eu_3Si_4H_2$, $Eu_3Si_4H_3$ and

$Eu_3Si_4H_4$ using an orthorhombic starting cell with Z = 2. No symmetry restrictions were applied during relaxation and the Findsym program [30] was used to check for symmetry of atom arrangements after relaxations. Forces were converged to better than 10^{-3} eV/Å. All materials were treated as non-magnetic and calculations were thus non spin-polarized.

2.6. Magnetic Measurements

Magnetization measurements were performed as a function of temperature using a Quantum Design MPMS SQUID magnetometer. M vs. T measurements were done both at low field (H = 4 kA/m) in order to determine the transition temperature of the samples, as well as in high field (H = 80 kA/m) in order to do a Curie-Weiss fit and estimate the effective bohrmagneton number (μ_{eff}) and Curie-Weiss temperature (Θ_{CW}) of the samples. M vs. H measurements were performed at 6K in the field range of ±7200 kA/m using a Quantum Design PPMS VSM magnetometer to determine the saturation magnetization as well as study the field dependence of the sample.

3. Results and Discussion

3.1. Hydrogenation behavior of Eu_3Si_4

Initially Eu_3Si_4 was exposed to a hydrogen atmosphere of 30 bar during 24 h at various temperatures in order to explore its hydrogen uptake behavior. Figure 2 shows selected PXRD patterns of reaction products. Pristine Eu_3Si_4 is remarkably susceptible to H uptake. As a matter of fact, kinetic barriers appear to be small because almost quantitative hydride formation is already observed at room temperature. At 100 °C and 200 °C a phase pure hydride was obtained. As will be explained later, we assign this hydride a composition $Eu_3Si_4H_{2+x}$. After hydrogenation at 300 °C a changed PXRD pattern is observed. Notably, several reflections seem to be split, which may indicate the formation of another hydride. When hydrogenating at temperatures above 300 °C, the crystallinity of products appears drastically reduced. Above 500 °C the product contained a substantial fraction $EuSi_2$, indicating H-induced oxidative decomposition. In this work we restrict ourselves to hydride phases obtained at low hydrogenation temperatures.

The diffraction patterns of $Eu_3Si_4H_{2+x}$ from 100 °C and 200 °C hydrogenations (samples $Eu_3Si_4\_H_2\_100C$ and $Eu_3Si_4\_H_2\_200C$, respectively) could be readily indexed in a body-centered orthorhombic cell with lattice parameters $a \approx 4.39$ Å, $b \approx 3.97$ Å, $c \approx 19.8$ Å. As a matter of fact, these parameters resemble those of the starting material Eu_3Si_4 (a = 4.6103(3) Å, b = 3.9574(1) Å, c = 18.2239(4) Å) [13] which suggests a close structural relationship between $Eu_3Si_4H_{2+x}$ and Eu_3Si_4. In-house PXRD data was not suitable for Rietveld refinement. PXRD data collected at a synchrotron were of vastly superior quality. Synchrotron PXRD patterns of the starting material and of the hydrogenated samples at 200 °C and 300 °C are shown in Figure 3. The pattern of the 300 °C product (sample $Eu_3Si_4\_H_2\_300C$) could be satisfactorily refined as a mixture of two orthorhombic phases. The first phase corresponds well to the hydride phase obtained in the 200 °C experiment. The only difference is that the c parameter appears slightly increased, from 19.81 to 19.86 Å. The second phase has a significantly increased a (~4.44 Å) and decreased c parameter (~19.58 Å). In the following we designate this phase as $Eu_3Si_4H_{\sim 2}$. Rietveld plots are shown as supporting information, Figure A1. The refinement results are contained in Tables 1 and 2 which also include the structure parameters of Eu_3Si_4 obtained from single crystal X-ray diffraction data, as reported in the literature [13]. There is good agreement between our parameters from powder refinement and the reported ones. Table A1 (supporting information) lists interatomic distances.

To elucidate the hydrogenation pathway and to possibly shed light into the formation of two phases when hydrogenating at 300 °C, an in-situ synchrotron PXRD experiment was performed. An overview of the results from this experiment can be seen in Figure 4 and Table 3. In contrast with the starting material used for the autoclave hydrogenation experiments, the Eu_3Si_4 sample synthesized for the in-situ experiment contained 6.1% $EuSi_2$ impurity (see Figure A2 and Table A2, supporting information). $EuSi_2$ does not absorb hydrogen and its presence did not hamper the analysis of data. The sample was subjected to a hydrogen atmosphere of 30 bar and subsequently heated to 400 °C at a rate of 5 °C/min,

dwelled for 5 min, and then cooled back to room temperature at a rate of 5 °C/min. (we remind that autoclave experiments applied a dwelling time of 24 h). A small but significant increase in the unit cell volume was noticed already at the start of the experiment. This indicates that Eu_3Si_4 absorbs hydrogen at room temperature, which is in agreement with the observation from the autoclave experiments (cf. Figure 2).

Upon heating, the actual transformation into a hydride phase started at 90 °C (after 0.25 h) – as indicated by the appearance of additional diffraction lines – and was completed at 140 °C (after 0.42 h), as indicated by the vanished reflections from Eu_3Si_4. The lattice parameters of the obtained hydride phase are $a \approx 4.4$ Å, $b \approx 4$ Å, $c \approx 19.9$ Å and thus (considering also thermal expansion) relate well to those of phase $Eu_3Si_4H_{2+x}$ obtained from the autoclave hydrogenations. Interestingly, upon heating beyond 180 °C (i. e. after 0.55 h) the *c* axis of the hydride phase contracted continuously, and was reduced by 0.6 Å when reaching 400 °C. The *c* axis contraction was paralleled by a slight expansion of the *a* axis (by 0.1 Å). This behavior was reversible upon cooling. Figure 5 depicts some detailed diffraction patterns. At 100 °C the pattern represents a phase mixture between Eu_3Si_4 and $Eu_3Si_4H_{2+x}$. Characteristic of the latter phase is the pair of reflections centered at $Q \approx 2.2$ Å^{-1} where Eu_3Si_4 has a single reflection. The diffraction patterns at 250 °C upon heating and cooling appear virtually identical. The pattern obtained at 400 °C yields the lattice parameters $a \approx 4.51$, $b \approx 4.0$, $c \approx 19.31$ Å, which are rather different from $Eu_3Si_4H_{2+x}$. Back at room temperature, values of the lattice parameters corresponded closely to those of $Eu_3Si_4H_{2+x}$ obtained in the autoclave experiment at 300 °C (i.e. sample $Eu_3Si_4\_H_2\_300C$, cf. Tables 1 and 3).

To sum up the salient observations with the in-situ experiment: there is an initial formation of a hydride in the temperature interval 90 – 140 °C, which upon further heating displays continuous variation of the *c* and *a* lattice parameters. These variations are reversible and the initially formed hydride is regained when cooling to room temperature. We conjecture that the initially formed phase corresponds to $Eu_3Si_4H_{2+x}$ obtained in autoclave hydrogenation experiments at 100 – 200 °C. At higher temperatures the hydrogen content is reduced and the phase seen at 400 °C in the in-situ experiment relates to second phase obtained in the 300 °C autoclave hydrogenation experiment, $Eu_3Si_4H_{\sim 2}$. For unknown reasons, a quenchable form of $Eu_3Si_4H_{\sim 2}$ can only be obtained after prolonged sintering at temperatures above 200 °C.

As a next step we investigated the thermal stability/desorption behavior of $Eu_3Si_4H_{2+x}$ by exposing parts of the sample $Eu_3Si_4\_H_2\_200C$ to a dynamic vacuum at elevated temperatures. Results are compiled in Figure A3 in the supporting information. The $Eu_3Si_4H_{2+x}$ phase was essentially maintained up to 200 °C. At 300 °C a changed diffraction pattern was obtained with a weaker crystallinity. Interestingly, there is strong indication that $Eu_3Si_4H_{\sim 2}$ partially formed during the 300 °C desorption experiment. Eu_3Si_4 did not reform in desorption experiments. Thus, the hydrogenation of Eu_3Si_4 to $Eu_3Si_4H_{2+x}$ is not reversible. Raman and IR spectra of Eu_3Si_4 and $Eu_3Si_4H_{2+x}$ are essentially featureless which indicates that both phases are metals.

Pressure composition isotherms (PCIs) measurements were attempted in order to determine the hydrogen content of $Eu_3Si_4H_{2+x}$. It was found that the sample absorbs hydrogen within a

single step (single plateau pressure) below 3 bar at 250 and 300 °C and the equilibrium pressure of the absorption plateau is very low and therefore below the detectable limits of the instrument. The maximum hydrogen capacity only reached 1.7 H/f.u. under these conditions, most probably due to kinetic limitation (see Figure A4). Diffraction analysis of the PCI samples conducted at 250 and 300 °C showed the presence of a phase mixture, analogous to the sample Eu_3Si_4_H_2_300C (Table A3). This is not surprising since the equilibrium times during PCI measurements (~2000 min) are similar to the dwelling time applied in the autoclave hydrogenation experiments (24 h), thus supporting the conjecture that the formation of a quenchable phase $Eu_3Si_4H_{\sim 2}$ is associated with a slow kinetics.

3.2. Structural variations and energetics of H incorporation

In the following we compare the structures of $Eu_3Si_4H_{2+x}$ and Eu_3Si_4 (cf. Tables 1-3). The *a* lattice parameter is the stacking direction of hexagon ring ribbons. With respect to Eu_3Si_4 this parameter is contracted by about 5% for $Eu_3Si_4H_{2+x}$ (from 4.62 to 4.4 Å) and by about 4% for $Eu_3Si_4H_{\sim 2}$. The *b* parameter (i.e. the direction of ribbons) is virtually unaffected upon hydride formation, whereas the *c* parameter increases considerably, from 18.24 to 19.81 – 19.87 Å for $Eu_3Si_4H_{2+x}$ and to 19.58 Å for $Eu_3Si_4H_{\sim 2}$. The associated volume increase of the unit cells are about 4.2 and 3.5%, respectively.

The high neutron capture cross section of Eu makes the application of neutron diffraction for structural analysis of $Eu_3Si_4H_{2+x}$ difficult, requiring samples with isotopically enriched ^{153}Eu. For identifying possible locations for H atoms, we therefore utilized our experience with $REGaH_{2-x}$ [10,11]. The precursor Zintl phases REGa crystallize with the CrB structure [15,16,17]. As discussed in the introduction, the Eu_3Si_4 structure can be considered built from slabs of CrB structure. The arrangement of Eu2 atoms in “Si” free layers corresponds to an array of edge sharing tetrahedra (cf. Figure 1). The centers of these tetrahedra are occupied in $REGaH_{2-x}$ by one kind of H atoms (H1). This is similar to hydrides with the ZrCuSiAs structure type (e.g. CeCoSiH) [31]. Assuming the same scenario for Eu_3Si_4 one arrives at an interstitial hydride $Eu_3Si_4H_2$. The centers of $Eu2_4$ tetrahedra corresponds to a site 4i (0,0,z) z ≈ 0.25 in space group *Immm*. The structure parameters of the $Eu_3Si_4H_2$ model were subsequently optimized by non spin polarized DFT calculations. To validate the simplified non spin polarized approach, we also subjected the Eu_3Si_4 structure to DFT optimization. The results are given in Tables 4 and A4. We note that the *Immm* structure of Eu_3Si_4 is excellently reproduced by DFT structure optimization (cf. Tables 1, 2, 4).

The DFT optimized structure for the $Eu_3Si_4H_2$ model (space group *Immm*) is shown in Figure 6. The incorporation of H into the $Eu2_4$ tetrahedral site in Eu_3Si_4 is clearly energetically favorable. The calculated energy for the reaction $Eu_3Si_4 + H_2 \rightarrow Eu_3Si_4H_2$ is -0.918 eV. However, the stabilization E/H = -0.459 eV is lower compared to $REGaH_{2-x}$ (E/H1 = -0.76 eV/H) because in the latter, H (in the equivalent H1 position) becomes situated in an environment of trivalent RE. Further, the DFT optimized structure of $Eu_3Si_4H_2$ structure shows evidently the experimentally observed trend in the lattice parameter variations, that is, a contracted *a*, constant *b* and expanded *c* parameter with respect to Eu_3Si_4. Importantly, the values are rather close to those of $Eu_3Si_4H_{\sim 2}$ from which we infer the approximate

composition of this phase. At the same time we are unable to provide an explanation as to why a quenchable form of $Eu_3Si_4H_{\sim 2}$ was only obtained in sintering experiments.

In contrast with the other RE metals, Eu can easily change between the di- and trivalent state. Several scenarios are possible when going from Eu_3Si_4 to $Eu_3Si_4H_2$. Importantly, in interstitial hydrides H behaves typically hydridic and, thus, interstitial hydride formation can be accompanied by both, oxidation of the polyanion and oxidation of Eu^{2+}. This is sketched in Figure 7. If Eu^{2+} was oxidized, a block $[Eu2_2H_2]$ would carry four positive charges and no changes are expected for the polyanion. If Eu^{2+} present in Eu_3Si_4 is not oxidized, a block $[Eu2_2H_2]$ carries two positive charges. Assuming charge balance, the Si hexagon chain becomes oxidized and may respond to this by developing π–bonding. This scenario is indicated when comparing the Si-Si distances in the DFT optimized structures of Eu_3Si_4 and $Eu_4Si_4H_2$ (Table A4). Both distances, Si1-Si2 and Si2-Si2 reduce slightly, by 0.02 – 0.03 Å, when going from Eu_3Si_4 to $Eu_3Si_4H_2$.

The considerably larger *c* parameter of $Eu_3Si_4H_{2+x}$ compared to $Eu_3Si_4H_{\sim 2}$ (and compared to the DFT optimized structure for $Eu_3Si_4H_2$) point to the incorporation of additional H in Eu_3Si_4, that is, a composition $Eu_3Si_4H_{2+x}$ is attained upon hydride formation below 200 °C. This situation would remind of REGa for which additional H, on the position H2, is inserted between Ga atoms of neighboring zigzag chains [10,11]. The H2 site is only partially occupied (2/3) in the hydrides $REGaH_{1.66}$. Importantly, H1 (fully occupied) and H2 are chemically different. The former is interstitial, primarily leading to an oxidation of the polyanion, the latter is a part of the polyanion [10].

Thus, again guided by REGa, we indentified the 4i position (0,0,~0.87) between two Si2 atoms of neighboring hexagon rings as a possible location for additional H. This position centers at the same time $Eu2_2Eu1$ triangles (cf. Figure 1a). The resulting Si_2Eu_3 trigonal bipyramidal environment is comparable to the Ga_2La_3 environment in the recently reported H-disordered hydride $LaGa_2D_{0.7}$, which is based on the AlB_2 structure type [32]. Subsequent DFT optimization of the structure parameters yielded a monoclinic structure for the hydride $Eu_3Si_4H_4$. The relaxed structure of this hydride is shown in Figure 8a. It features a polyanion $[Si1_2Si2_2H2_2]^{4-}$ in which H2 is regularly bonded to Si2 (d(Si2-H2) = 1.61 Å). At the same time, planar hexagon rings corrugate slightly and attain a chair conformation. The situation is strikingly similar to recently discovered $BaSiH_{2-x}$ and $SrSiH_{5/3-x}$ with polyanionic zigzag chains $[SiH]^-$ and ribbons $[Si_2H]^{2-}$, respectively [8,9]. In these compounds (calculated) Si-H distances are in a range 1.64 to 1.66 Å.

The reaction energy for the step $Eu_3Si_4H_2 + H_2 \rightarrow Eu_3Si_4H_4$ is still negative, -0.395 eV, but it is clear that the H2 position is far less favorable compared to H1. The structure of $Eu_3Si_4H_4$ is monoclinic, but the lattice metrics is close to orthorhombic. The monoclinic angle of a body centered lattice, which is preferably used when comparing to the *Immm* structures of Eu_3Si_4 and $Eu_3Si_4H_2$, is 91.9° (cf. Table 4). The *c* lattice parameter of $Eu_3Si_4H_4$ is considerably increased compared to $Eu_3Si_4H_2$, to 19.88 Å, whereas the *a* and *b* parameters are essentially the same. Thus, it appears that a closer agreement to the experimental values was obtained (cf. Table 1). We also considered an ordered model $Eu_3Si_4H_3$ with half of the Si2 atoms

terminated by H2 type atoms. Its DFT optimized structure, which also is monoclinic, is shown in Figure 8b. The increase of the *c* parameter with respect to Eu_3Si_4 is less pronounced (19.61 Å).

The monoclinic symmetry of the calculated models $Eu_3Si_4H_4$ and $Eu_3Si_4H_3$ is a consequence of the puckering of hexagon layers. The symmetry reduction is clearly not observed in the PXRD pattern of e.g. $Eu_3Si_4H_2$_H_2_200C (cf. Figures 3 and A1). Therefore it can be concluded that the additional H in $Eu_3Si_4H_{2+x}$ probably incorporates in a more complicated, disordered, fashion. A similar situation has been described for $LaGa_2D_{0.7}$ [32].

3.3. H-induced magnetic property changes

The ZFC and FC magnetization of Eu_3Si_4 and $Eu_3Si_4H_{2+x}$ (sample Eu_3Si_4_H_2_200C) as a function of temperature in an applied field of 4 kA/m is shown in Figure 9a. The Zintl phase Eu_3Si_4 has two noteworthy features, a sharp increase in the magnetization at 120 K and another pronounced feature at about 40 K. In Ref. [13] the same behavior was observed, and the authors suggested a ferromagnetic ordering at 117 K for the Eu2 site and a consecutive ferromagnetic ordering of the Eu1 site at about 40 K. However, with a weak antiferromagnetic coupling between the two substructures which gives rise to a ferrimagnetic total structure at low temperatures. Upon hydrogenation it can be observed that the ferromagnetic transition at 120 K disappears, indicating that the hydrogenation disrupts the ordering of the Eu2 moments at 120 K. Since SQUID magnetometry is very sensitive to magnetic impurities (especially ferromagnetic ones) it is also clear that there is no trace of the original ferromagnetic Eu_3Si_4 phase in the hydride sample.

The ZFC and FC thermomagnetic curves for the $Eu_3Si_4H_{2+x}$ sample in Figure 9a indicates a para- to antiferromagnetic transition at about 40 K. However, with some uncompensated spins in the antiferromagnetic phase giving rise to an excess moment as seen from the separation of the ZFC and FC curves below the transition temperature. The magnetization as a function of field behavior at 6 K is complex and exhibits a second magnetic hysteresis loop at high fields (above 3000 kA/m), see Figure 9b). A similar behavior to the data presented in Figure 9b has been observed in single crystals of the antiferromagnet $UIrSi_3$, which crystallizes in the tetragonal $BaNiSn_3$ structure type [33]. The magnetic moments in $UIrSi_3$ order ferromagnetically in the *ab* plane with the moments aligned along the *c* axis. The ferromagnetic planes order then antiferromagnetically with respect to each other, yielding a net antiferromagnetic structure. Upon application of a sufficiently large magnetic field along the *c* axis (easy axis), $UIrSi_3$ exhibits a metamagnetic transition to a ferromagnetic configuration. No metamagnetic transition was observed upon application of the magnetic field along the *a* axis. Even though the behavior observed in $UIrSI_3$ agrees well with the data presented in Figure 9b (if the polycrystallinity of the $Eu_3Si_4H_{2+x}$ sample is taken into account), it cannot with certainty be concluded that this is the origin of the observed effect from the collected data. From Curie-Weiss fits it was found that $p_{eff} \approx 7.5\ \mu_B$ (~7.2 for Eu_3Si_4 and ~7.7 for the hydrogenated sample), indicating $4f^7$ Eu^{2+} for both samples (Eu^{2+} ~8 and Eu^{3+} ~3.4 μ_B). The Curie-Weiss temperatures (Ω_{CW}) are ~110 and ~5 K for Eu_3Si_4 and $Eu_3Si_4H_{2+x}$

respectively. The drastic change in Ω_{CW} further underlines the disruptive effect that hydrogen has on the magnetic interaction in Eu_3Si_4.

4. Conclusions

Eu_3Si_4 absorbs hydrogen already at room temperature when exposing the material to a hydrogen atmosphere of 30 bar. Structural analysis by a combination of X-Ray powder diffraction and DFT modeling suggests that at temperatures up to 200 °C a hydride $Eu_3Si_4H_{2+x}$ is formed, whereas sintering at higher temperatures (300 °C) affords a hydride with lower hydrogen content, $Eu_3Si_4H_{\sim 2}$. $Eu_3Si_4H_{2+x}$ desorbs H irreversibly above T = 200 °C. The ferromagnetic properties of Eu_3Si_4 are effectively quenched upon hydrogenation to $Eu_3Si_4H_{2+x}$. The effective bohrmagneton number of $Eu_3Si_4H_{2+x}$ is close to that of Eu_3Si_4 above T_c, indicating that Eu possesses the same oxidation state (i.e. +2) in both systems.

Acknowledgement. This work has been supported by the Swedish research council and the NordForsk project “Neutrons for multifunctional hydrides (FunHy)”.

References

[1] S. M. Kauzlarich, Chemistry, Structure, and Bonding of Zintl Phases and Ions, Wiley, 1996.

[2] R. Nesper, The Zintl-Klemm Concept - A Historical Survey, Z. Anorg. Allg. Chem. 640 (2014) 2639–2648. doi:10.1002/zaac.201400403.

[3] S. C. Sevov, Zintl phases, in: J. H. Westbrook, R. L. Fleischer (Eds.), Intermetallic Compounds: Principles and Practice, John Wiley and Sons Ltd, 2002, pp. 113–132.

[4] U. Häussermann, V. F. Kranak, K. Puhakainen, Hydrogenous Zintl Phases: Interstitial Versus Polyanionic Hydrides, in: T. F. Fässler (Ed.), Zintl phases: Principles and recent developments, Structure and Bonding 139 (2011), 143–161. doi: 10.1007/430_2010_20.

[5] U. Häussermann, Coexistence of hydrogen and polyanions in multinary main group element hydrides, Z. Kristallogr. 223 (2008) 628–635. doi:10.1524/zkri.2008.1016.

[6] T. Björling, D. Noreus, K. Jansson, M. Andersson, E. Leonova, M. Eden, U. Hålenius, U. Häussermann, SrAlSiH: A Polyanionic Semiconductor Hydride, Angew. Chem. Int. Ed. 44 (2005) 7269–7273. doi:10.1002/anie.200502090.

[7] M. H. Lee, T. Björling, B. C. Hauback, T. Utsumi, D. Moser, D. Bull, D. Noreus, O. F. Sankey, U. Häussermann, Crystal structure, electronic structure, and vibrational properties of MAlSiH (M=Ca,Sr,Ba): Hydrogenation-induced semiconductors from the AlB2-type alloys MAlSi, Phys. Rev. B 78 (2008) 195209. doi:10.1103/PhysRevB.78.195209.

[8] H. Auer, R. Guehne, M. Bertmer, S. Weber, P. Wenderoth, T. C. Hansen, J. Haase, H. Kohlmann, Hydrides of Alkaline Earth–Tetrel (AeTt) Zintl Phases: Covalent Tt–H Bonds from Silicon to Tin, Inorg. Chem. 56 (2017) 1061–1071. doi:10.1021/acs.inorgchem.6b01944.

[9] H. Auer, R. Schlegel, O. Oeckler, H. Kohlmann, Structural and Electronic Flexibility in Hydrides of Zintl Phases with Tetrel – Hydrogen and Tetrel – Tetrel Bonds, Angew. Chem. Int. Ed. 56 (2017) 12344–12347. doi:10.1002/anie.201706523.

[10] J. Ångström, R. Johansson, T. Sarkar, M. H. Sørby, C. Zlotea, M. S. Andersson, P. Nordblad, R. H. Scheicher, U. Häussermann, M. Sahlberg, Hydrogenation-Induced Structure and Property Changes in the Rare-Earth Metal Gallide NdGa: Evolution of a [GaH]2- Polyanion Containing Peierls-like Ga-H Chains, Inorg. Chem. 55 (2016) 345–352. doi:10.1021/acs.inorgchem.5b02485.

[11] R. Nedumkandathil, V. F. Kranak, R. Johansson, J. Angström, O. Balmes, M. S. Andersson, P. Nordblad, R. H. Scheicher, M. Sahlberg, U. Häussermann, Hydrogenation induced structure and property changes in GdGa, J. Solid. State Chem. 239 (2016) 184–191. doi:10.1016/j.jssc.2016.04.028.

[12] H. Auer, R. Nedumkandathil, U. Häussermann, H. Kohlmann, The Hydrogenation of the Zintl Phase NdGa Studied by in situ neutron diffraction, Z. Anorg. Allg. Chem. 645 (2019) 175–181. doi:10.1002/zaac.201800459.

[13] F. Weitzer, Y. Prots, W. Schnelle, K. Hiebl, Y. Grin, The novel silicide Eu3Si4: Structure, chemical bonding, magnetic behavior and electrical resistivity, J. Solid State Chem. 177 (2004) 2115–2121. doi:10.1016/j.jssc.2004.02.013.

[14] The structure refinement reported in ref. [13] described one of the Si atoms (2b) Si2 with a split position, indicating a slight corrugation of the Si hexagon rings. In the discussion of the experimental Eu_3Si_4 structure in this work an idealized structure with planar hexagon rings is assumed. In this structure Si2 is located on a position 4i (0,0.4360).

[15] B. Barbara, Nguyen-Van-Nhung, E. Siaud, Magnetic properties of rare earth-gallium equiatomic compounds, CR. Acad. Sci B 274 (1972) 1053–1056.

[16] H. Fujii, N. Shohata, T. Okamoto, E. Tatsumoto, Magnetic Properties of Rare Earth Gallium Compounds RGa, J. Phys. Soc. Jpn. 31 (1971) 1592–1592. doi:10.1143/JPSJ.31.1592.

[17] N. Shohata, Magnetic Properties of Rare Earth Gallium Intermetallic Compounds, J. Phys. Soc. Jpn. 42 (1977) 1873–1880. doi:10.1143/JPSJ.42.1873.

[18] A. P. Hammersley, S. O. Svensson, M. Hanfland, A. N. Fitch, D. Hausermann, Two-dimensional detector software: From real detector to idealised image or two-theta scan, High Pressure Res. 14 (1996) 235–248. doi:10.1080/08957959608201408.

[19] H. M. Rietveld, A profile refinement method for nuclear and magnetic structures, J. Appl. Crystallogr. 2 (1969) 65–71. doi:10.1107/S0021889869006558.

[20] R.-C. Juan, Fullprof: A Program for Rietveld Refinement and Pattern Matching Analysis, Abstract of the Satellite Meeting on Powder Diffrac- tion of the XV Congress of the IUCr, Toulouse, France 127 (1990).

[21] P. Norby, Hydrothermal Conversion of Zeolites: An in Situ Synchrotron X-ray Powder Diffraction Study, J. Am. Chem. Soc. 119 (1997) 5215–5221. doi:10.1021/ja964245g.

[22] A. A. Coelho, Computer programs TOPAS and TOPAS-Academic: an optimization program integrating computer algebra and crystallographic objects written in C ++ 210–218 (2018). doi:10.1107/S1600576718000183.

[23] G. Kresse, J. Hafner, Ab initio molecular dynamics for liquid metals, Phys. Rev. B 47 (1993) 558–561. doi:10.1103/PhysRevB.47.558.

[24] G. Kresse, J. Furthmuller, Efficiency of ab-initio total energy calculations for metals and semiconductors using a plane-wave basis set, Comput. Mater. Sci. 6 (1996) 15–50. doi:10.1016/0927- 0256(96)00008-0.

[25] P. E. Blöchl, Projector augmented-wave method, Phys. Rev. B 50 (1994) 17953–17979. doi:10.1103/PhysRevB.50.17953.

[26] G. Kresse, D. Joubert, From ultrasoft pseudopotentials to the projector augmented-wave method, Phys. Rev. B 59 (1999) 1758–1775. doi:10.1103/PhysRevB.59.1758.

[27] J. P. Perdew, K. Burke, M. Ernzerhof, Generalized Gradient Approximation Made Simple, Phys. Rev. Lett. 77 (1996) 3865–3868. doi:10.1103/PhysRevLett.77.3865.

[28] J. P. Perdew, K. Burke, M. Ernzerhof, Generalized Gradient Approximation Made Simple [erratum], Phys. Rev. Lett. 78 (1997) 1396–1396. doi:10.1103/PhysRevLett.78.1396.

[29] H. J. Monkhorst, J. D. Pack, Special points for Brillouin-zone integrations, Phys. Rev. B 13 (1976) 5188–5192. doi:10.1103/PhysRevB.13.5188.

[30] H. T. Stokes, D. M. Hatch, FINDSYM: program for identifying the space-group symmetry of a crystal, J. Appl. Crystallogr. 38 (2005) 237–238. doi:10.1107/S0021889804031528.

[32] R. Pöttgen, D. Johrendt, Materials with ZrCuSiAs-type Structure, Z. Naturforsch. 63b (2008) 1135–1148. doi:10.1515/znb- 2008-1001.

[31] A. Werwein, C. Benndorf, M. Bertmer, A. Franz, O. Oeckler, H. Kohlmann, Hydrogenation properties of $LnAl_2$ (Ln = La, Eu, Yb), $LaGa_2$, $LaSi_2$ and the crystal structure of $LaGa_2H_{0.71(2)}$, Crystals 9 (2019) 1–12. doi:10.3390/cryst9040193.

[33] J. Valenta, F. Honda, M. Valiska, P. Opletal, J. Kastil, M. Misek, M. Divis, L. Sandratskii, J. Prchal, V. Sechovsky, Antiferromagnetism and phase transitions in noncentrosymmetric UIrSi3, Phys. Rev. B 97 (2018) 144423. doi.org/10.1103/PhysRevB.97.144423

Figures

Figure 1. a) Idealized crystal structure of Eu_3Si_4 (space group *Immm*) with polyanionic ribbons of planar hexagon rings projected approximately along the *a* (left) and the *b* (right) direction [13,14]. The arrangement of Eu2 atoms into arrays of edge condensed tetrahedra and the trigonal prismatic coordination of Eu2 around Si atoms are emphasized. b) Relation of the CrB and Eu_3Si_4 structures. Eu and Si atoms are depicted as grey and red circles, respectively.

Figure 2. PXRD patterns (Cu $K\alpha_1$) of products from the hydrogenation of Eu_3Si_4 at p = 30 bar during 24 h experiments at room temperature, 100 °C, 200 °C, and 300 °C. The pattern of the Eu_3Si_4 starting material is shown as black line.

Figure 3. Synchrotron PXRD patterns (λ = 0.2073 Å) for Eu_3Si_4 and products obtained from 24 h hydrogenations at 200 °C ($Eu_3Si_4\_H_2\_200C$) and 300 °C ($Eu_3Si_4\_H_2\_300C$).

Figure 4. a) Densiometric view of diffraction patterns during in-situ synchrotron measurements. b) Unit cell parameters of the hydride phase obtained from sequential Rietveld refinements.

Figure 5. Selected diffraction patterns during different stages of hydrogenation (as shown in Figure 4). Reflections from the $EuSi_2$ impurity phase are marked with asterisks (*).

Figure 6. DFT optimized crystal structure model for $Eu_3Si_4H_2$.

Figure 7. Different scenarios for products from Eu_3Si_4 hydrogenation.

Figure 8. DFT optimized crystal structure models for $Eu_3Si_4H_4$, $Eu_3Si_4H_3$.

Figure 9. a) Zero field cooled and field cooled curves for Eu_3Si_4 and $Eu_3Si_4H_{2+x}$ in an applied magnetic field H = 4 kA/m. b) Magnetization as a function of applied magnetic field for Eu_3Si_4 and $Eu_3Si_4H_{2+x}$ at 6 K.

Tables:

Ferromagnetic Eu_3Si_4 absorbs hydrogen to yield hydrides $Eu_3Si_4H_{2+x}$ with quenched ferromagnetism.

Table 1: Crystallographic information for Eu_3Si_4 and hydrogenated Eu_3Si_4 samples from Rietveld refinements.

SG: *Immm*	*a* (Å)	*b* (Å)	*c* (Å)	*V* (Å^3)	R_{bragg}	R_f	χ^2
Eu_3Si_4 (ref. [13])	4.6164(4)	3.9583(3)	18.229(1)	333.10(7)			
Eu_3Si_4	4.61499(9)	3.95949(8)	18.2361(5)	333.23(1)	4.49	3.71	0.410
Eu_3Si_4_H_2_200C	4.40055(5)	3.97166(5)	19.8098(3)	346.225(8)	4.8	3.68	0.831
Eu_3Si_4_H_2_300C							0.941
$Eu_3Si_4H_{2+x}$ 64(1) %	4.40247(7)	3.97478(9)	19.8646(5)	347.61(1)	5.35	4.06	
$Eu_3Si_4H_{\sim 2}$ 35(7)%	4.4391(1)	3.9778(1)	19.5784(8)	345.72(2)	7.22	6.01	

Table 2: Atomic coordinates and isotropic displacement parameters for Eu_3Si_4 and hydrogenated Eu_3Si_4 samples.

	Atom	Wyck	*x*	*y*	*z*	B(Å^2)
Eu_3Si_4 (ref. [13])	Eu1	2*a*	0	0	0	0.51(3)
	Eu2	4*j*	½	0	0.31500(6)	0.54(2)
	Si1	4*i*	0	0	0.4360(4)	0.6(1)
	Si2	4*j*	½	0	0.1377(3)	0.7(1)
Eu_3Si_4	Eu1	2*a*	0	0	0	1.03(2)
	Eu2	4*j*	½	0	0.31487(0)	1.03(2)
	Si1	4*i*	0	0	0.43667(4)	1.69(7)
	Si2	4*j*	½	0	0.13800(4)	1.69(7)
Eu_3Si_4_H_2_200C	Eu1	2*a*	0	0	0	0.909(5)
	Eu2	4*j*	½	0	0.31019(0)	0.909(5)
	Si1	4*i*	0	0	0.440164)	1.03(1)
	Si2	4*j*	½	0	0.12066(4)	1.03(1)
Eu_3Si_4_H_2_300C $Eu_3Si_4H_{2+x}$	Eu1	2*a*	0	0	0	0.601(7)
	Eu2	4*j*	½	0	0.31014(0)	0.601(7)
	Si1	4*i*	0	0	0.44593(1)	0.23(2)
	Si2	4*j*	½	0	0.12907(1)	0.23(2)
Eu_3Si_4_H_2_300C $Eu_3Si_4H_{\sim 2}$	Eu1	2*a*	0	0	0	1.9(2)
	Eu2	4*j*	½	0	0.31190(0)	1.9(2)
	Si1	4*i*	0	0	0.43072(2)	1.4(4)
	Si2	4*j*	½	0	0.11365(2)	1.4(4)

Table 3: Cell parameters obtained by sequential Rietveld refinements of in-situ data.

	Time (h)	*a* (Å)	*b* (Å)	*c* (Å)	*V* (Å^3)
Eu_3Si_4 (93.9%)		4.6146(4)	3.9572(3)	18.229(2)	332.90
Start	0	4.6193(1)	3.96156(9)	18.2454(5)	333.88
250 °C	0.78	4.4371(3)	3.9836(2)	19.785(1)	349.73
400 °C	1.33	4.5085(2)	3.9968(2)	19.3128(8)	348.02
250 °C	1.87	4.4397(2)	3.9842(2)	19.759(1)	349.53
End	2.63	4.4013(2)	3.9756(2)	19.857(1)	347.47

Table 4: Parameters of DFT optimized structures.

	Atom	Wyck	*x*	*y*	*z*	*a*, *b*, *c* (Å)	*V*(Å^3)
	Eu1	2*a*	0	0	0	4.5817	
Eu_3Si_4	Eu2	4*j*	½	0	0.3156	3.9445	329.25
Immm (71)	Si1	4*i*	0	0	0.4351	18.2180	
	Si2	4*j*	½	0	0.1383		
	Eu1	2*a*	0	0	0	4.4208	
$Eu_3Si_4H_2$	Eu2	4*j*	½	0	0.3064	3.9716	
Immm (71)	Si1	4*i*	0	0	0.4399	19.3803	340.27
	Si2	4*j*	½	0	0.1259		
	H1	4*i*	0	0	0.2567		
	Eu1	2*e*	0.2396	¼	0.2529	4.3903	
	Eu21	2*e*	0.7364	¼	-0.0585	3.9794	
	Eu22	2*e*	0.7483	¼	0.5560	19.6102	
$Eu_3Si_4H_3$	Si11	2*e*	0.2918	¼	0.8069	β = 90.9°	
$P2_1/m$ (11)	Si12	2*e*	0.2444	¼	0.6876		342.56
	Si21	2*e*	0.7690	¼	0.1273		
	Si22	2*e*	0.7492	¼	0.3768		
	H11	2*e*	0.2414	¼	-0.0045		
	H12	2*e*	0.2458	¼	0.5068		
	H2	2*e*	0.1366	¼	0.1286		
$Eu_3Si_4H_4$	Eu1	2*a*	0	0	0	4.4192	
*I*2/*m* (12)	Eu2	4*i*	0.4836	0	0.6916	3.9625	
	Si1	4*i*	0.0551	0	0.5593	19.8895	348.10
	Si2	4*i*	0.5204	0	0.8765	β = 91.9°	
	H1	4*i*	-0.0070	0	0.7450		
	H2	4*i*	0.1162	0	0.1231		

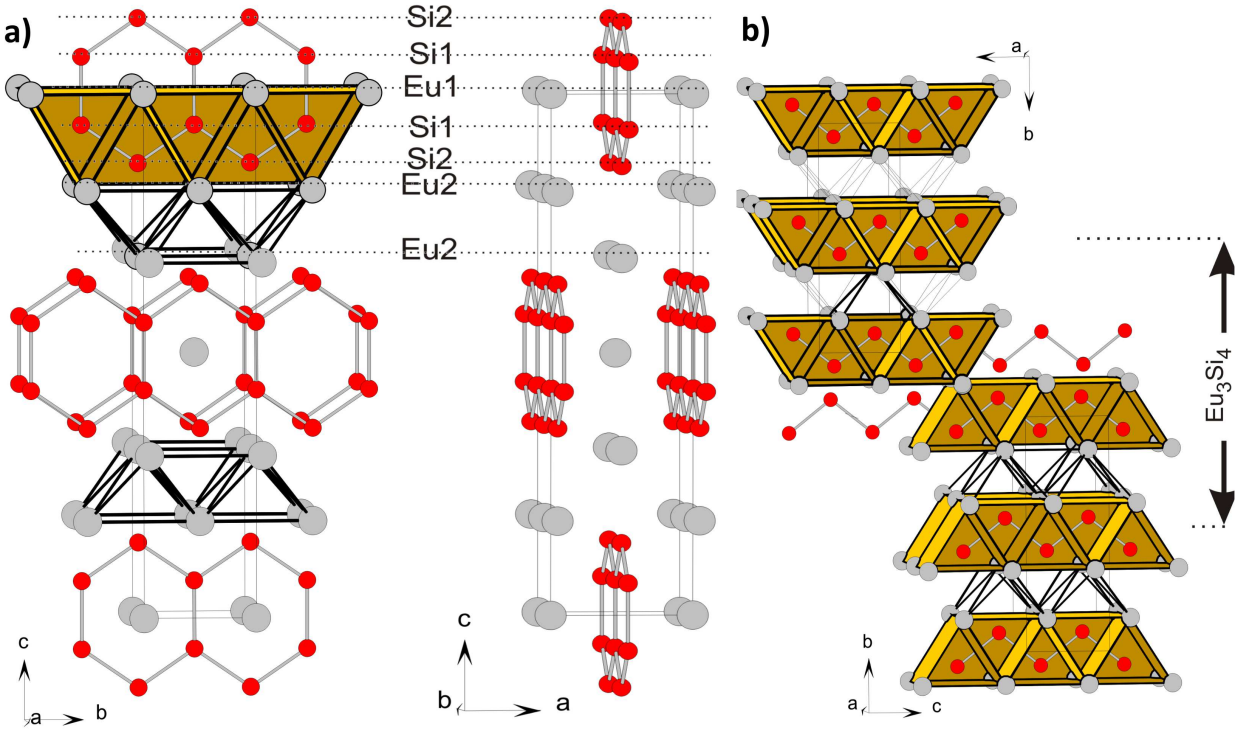

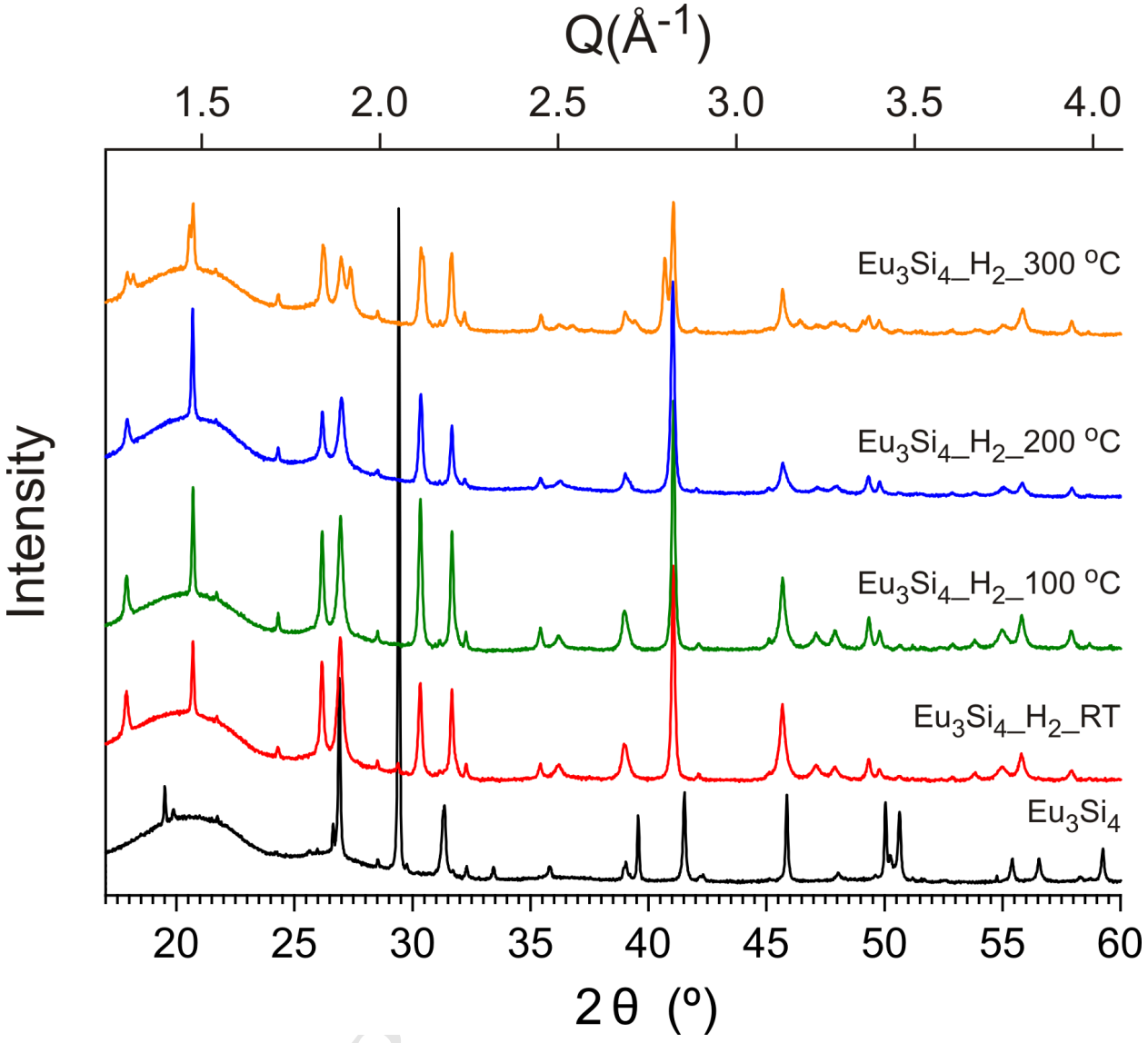
Q(Å-1)
1.5
2.0
2.5
3.0
3.5
4.0
Intensity
Eu3Si4_H2_300 °C
Eu3Si4_H2_200 °C
Eu3Si4_H2_100 °C
Eu3Si4_H2_RT
Eu3Si4
20
25
30
35
40
45
50
55
60
2θ (°)

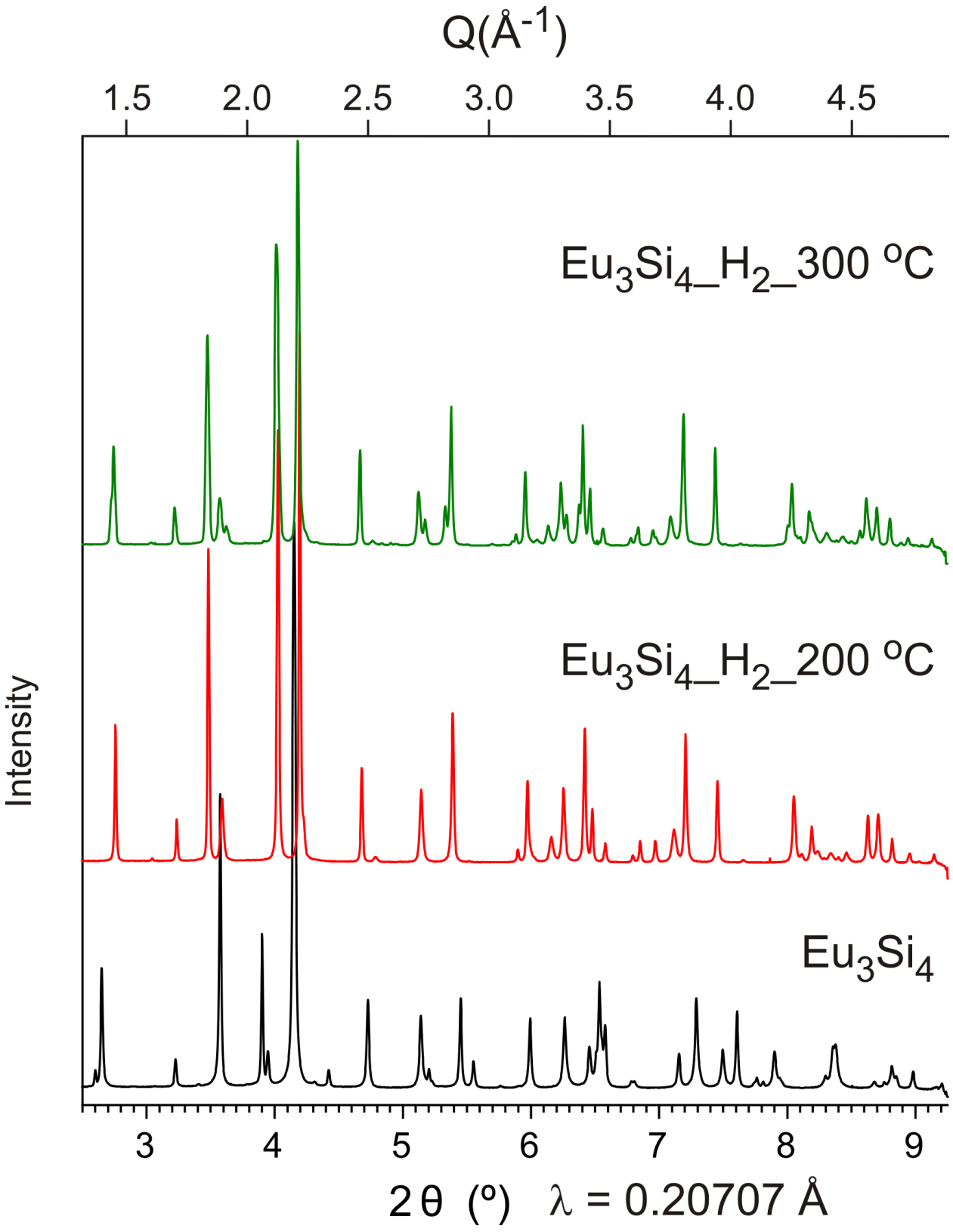
Q(Å-1)
1.5
2.0
2.5
3.0
3.5
4.0
4.5
Eu3Si4_H2_300 ºC
Eu3Si4_H2_200 ºC
Eu3Si4
Intensity
3
4
5
6
7
8
9
2θ (º) λ = 0.20707 Å

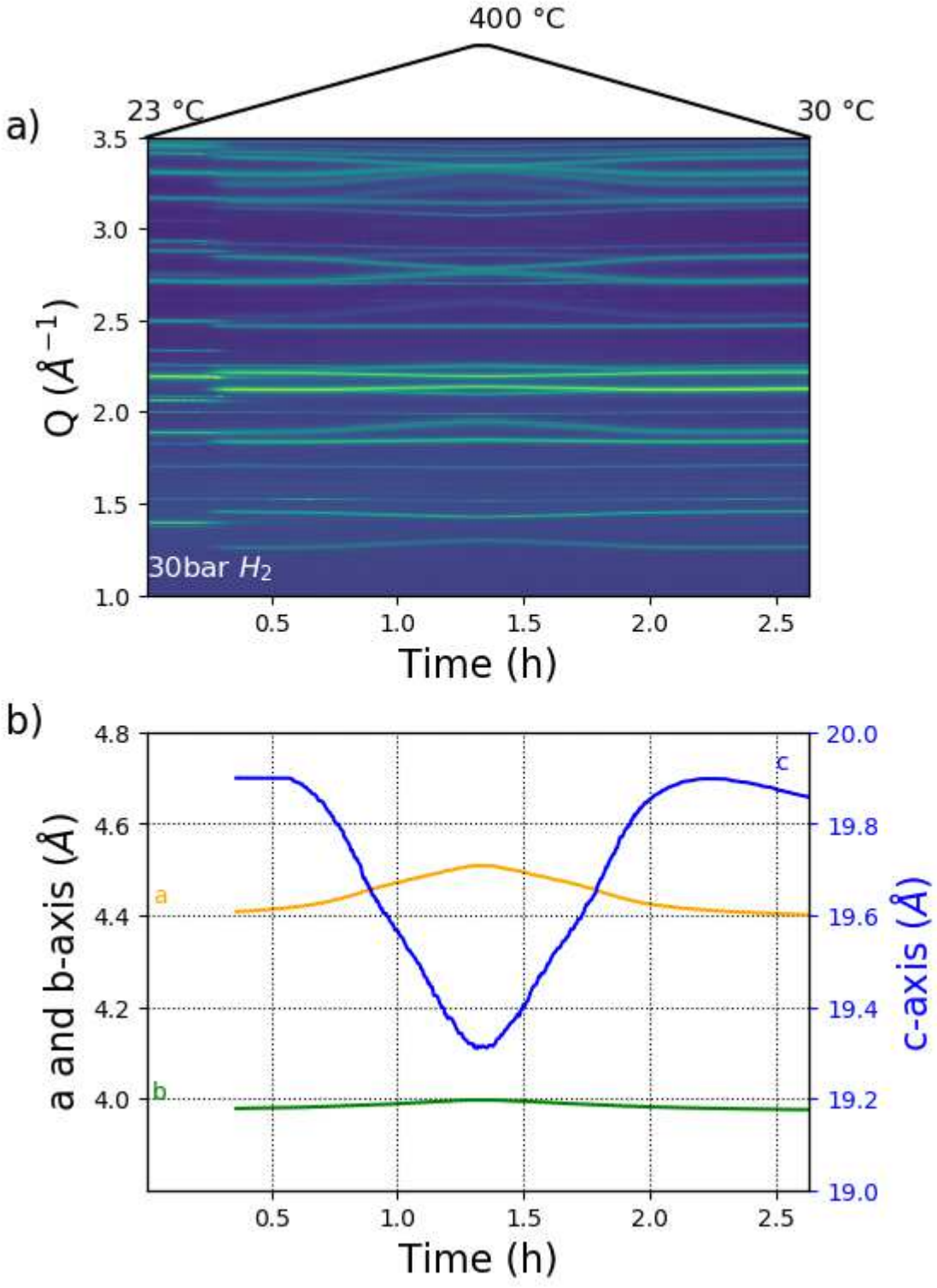
a)
400 °C
23 °C
30 °C
3.5
3.0
2.5
2.0
1.5
1.0
Q (Å^{-1})
30bar H_2
0.5
1.0
1.5
2.0
2.5
Time (h)
b)
4.8
4.6
4.4
4.2
4.0
a and b-axis (Å)
a
b
c
20.0
19.8
19.6
19.4
19.2
19.0
c-axis (Å)
0.5
1.0
1.5
2.0
2.5
Time (h)

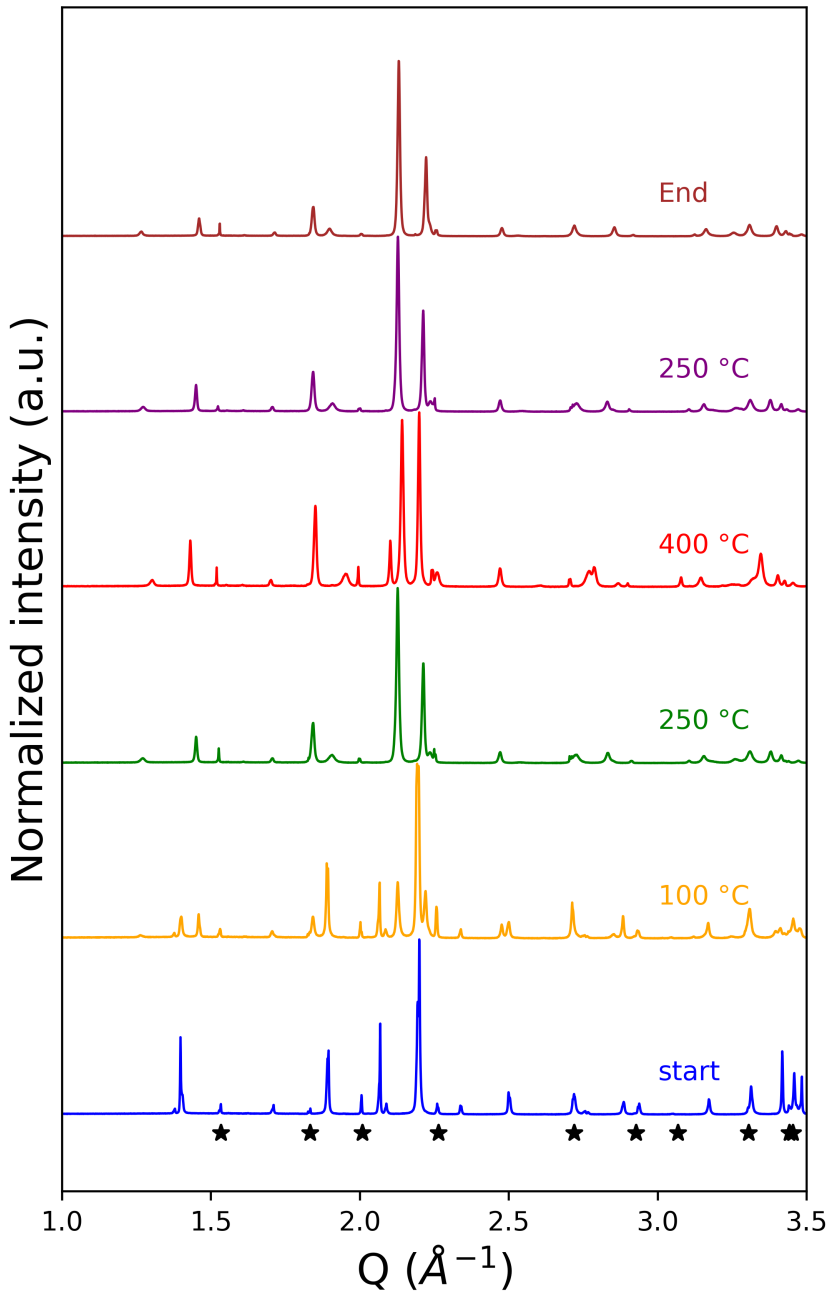
End
250 °C
400 °C
250 °C
100 °C
start
Normalized intensity (a.u.)
1.0
1.5
2.0
2.5
3.0
3.5
Q (Å^{-1})

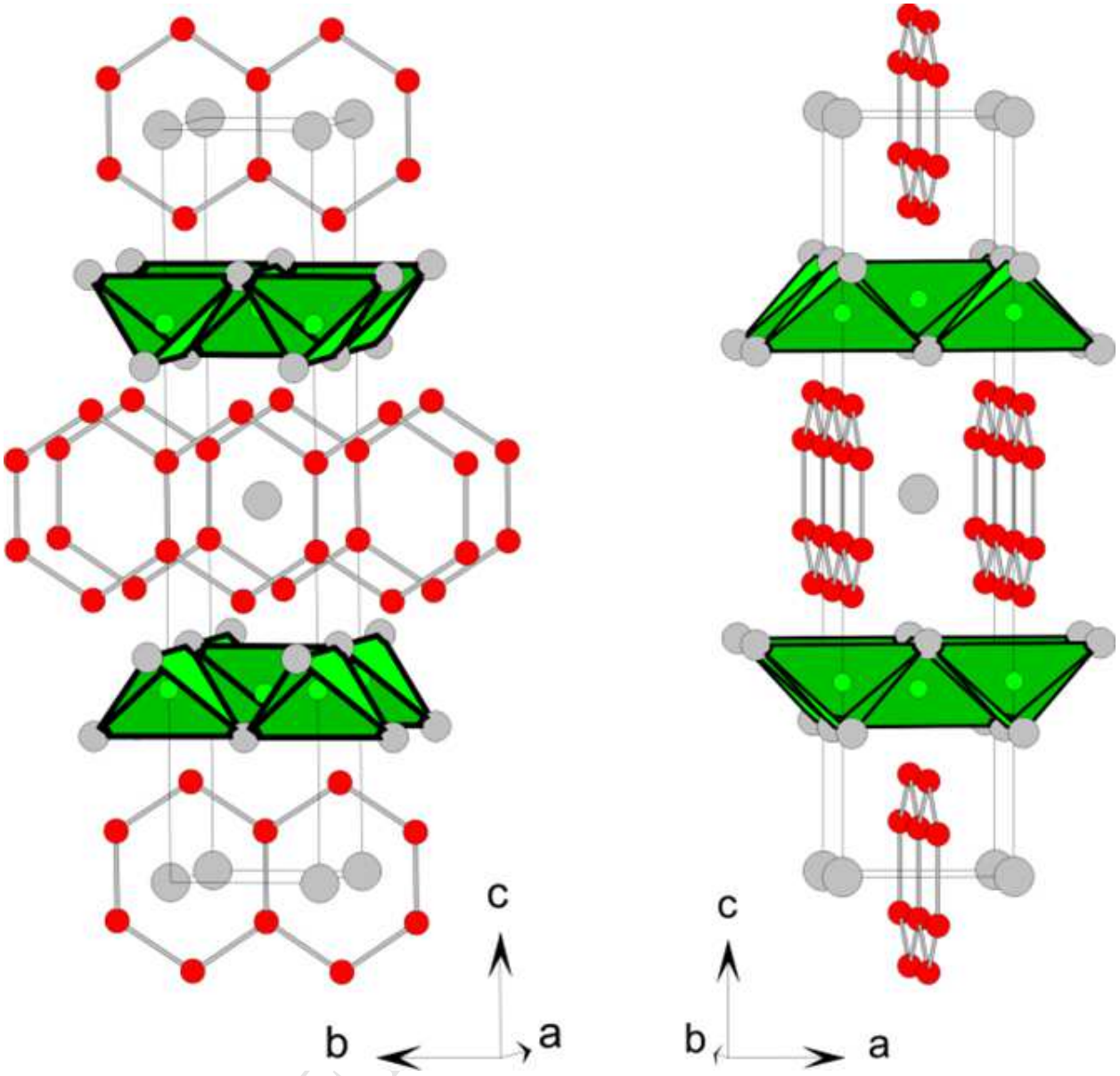

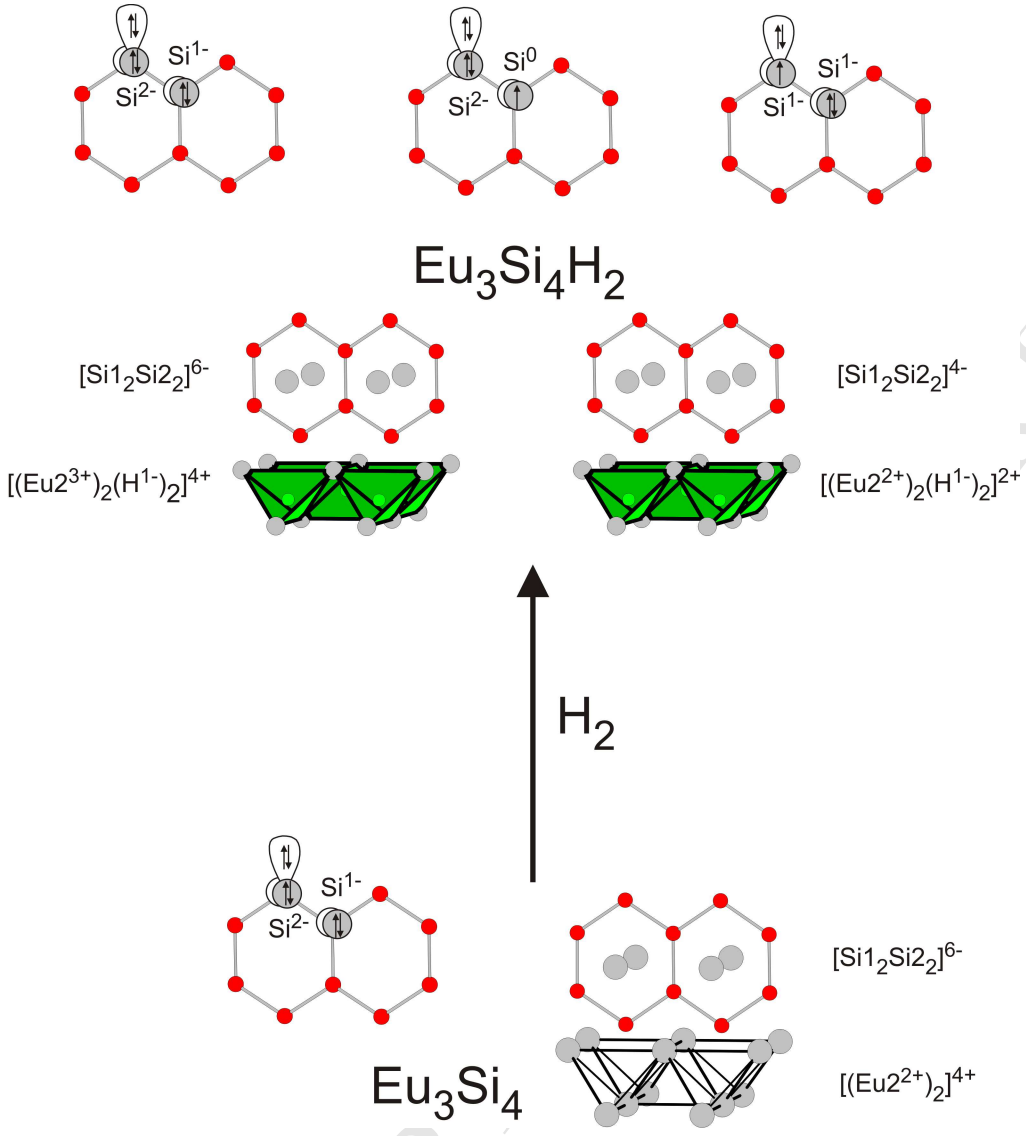

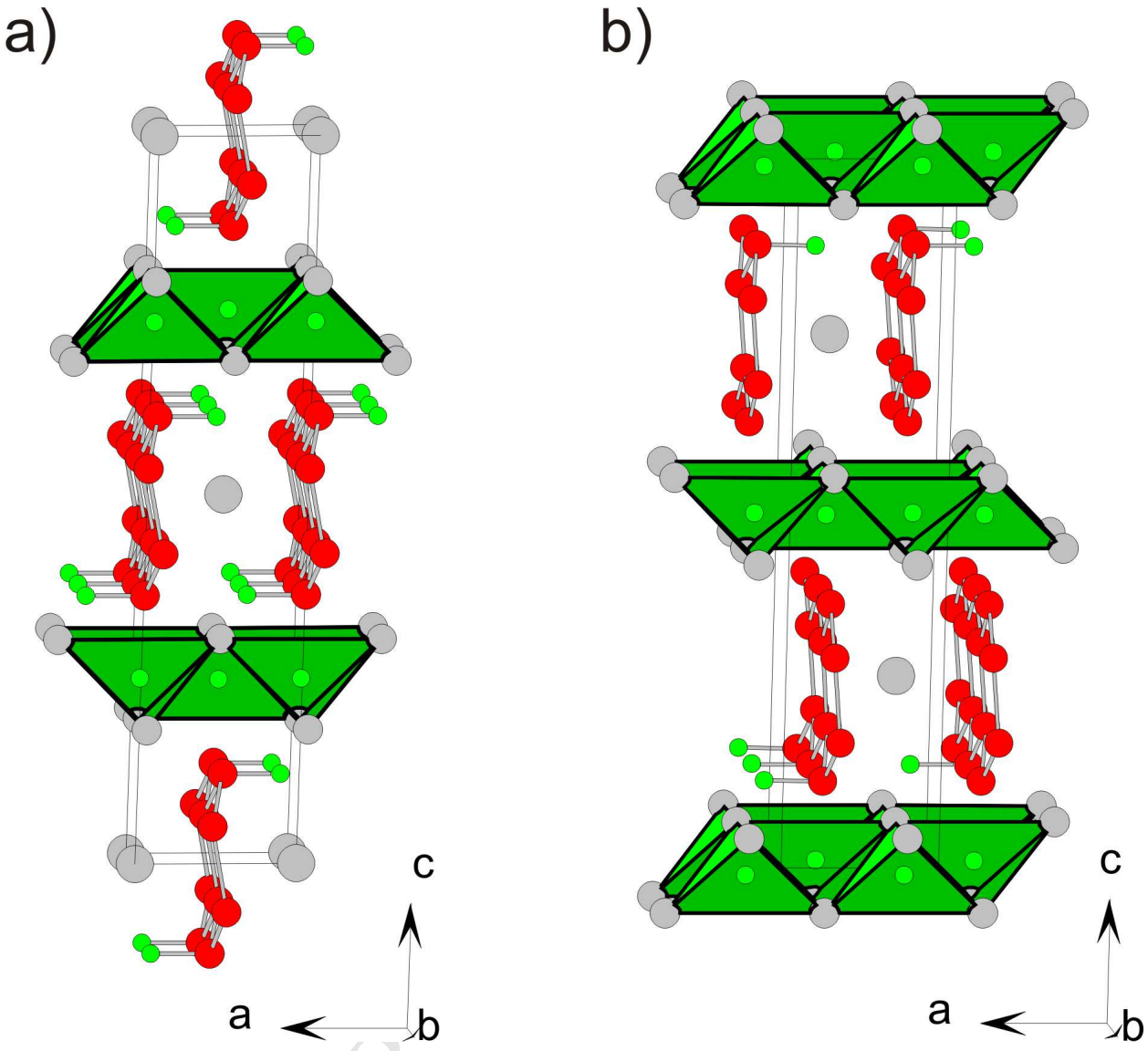

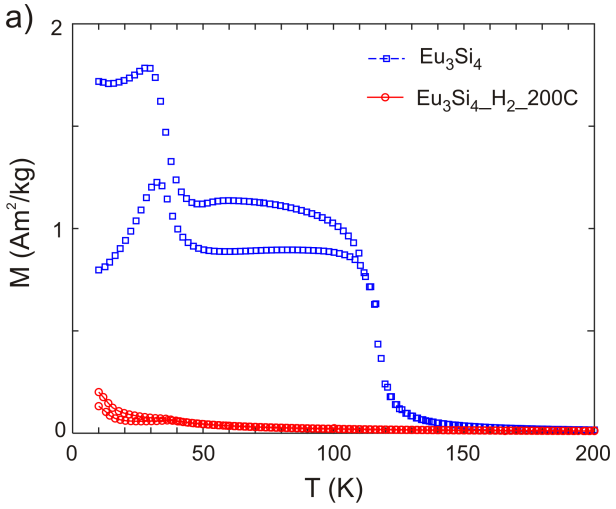

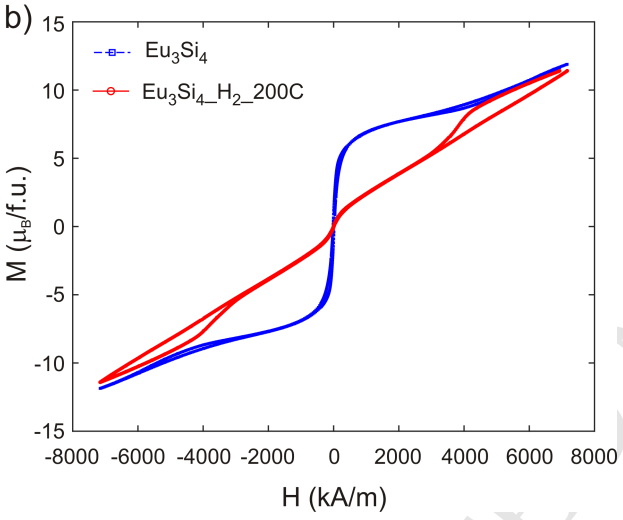

Research highlights:

- Eu_3Si_4 absorbs hydrogen at room temperature when using pressures of about 30 bar.
- H-incorporation in Eu_3Si_4 leads to the formation of hydrides $Eu_3Si_4H_{2+x}$ ($x<2$).
- H-incorporation in Eu_3Si_4 does not alter the oxidation state of Eu (II).
- H-incorporation in Eu_3Si_4 quenches effectively its ferromagnetism.